PHYSICAL REVIEW B VOLUME 35, NUMBER 13 1 MAY 1987

Magnetic structure of Dy-Y superlattices

R. W. Erwin and J. J. Rhyne
Reactor Division, National Bureau of Standards, Gaithersburg, Maryland 20899

M. B. Salamon, J. Borchers, Shantanu Sinha, R. Du, J. E. Cunningham,* and C. P. Flynn
Department of Physics and Materials Research Laboratory, University of Illinois at Urbana-Champaign, Urbana, Illinois 61801
(Received 3 November 1986)

Two samples of Dy-Y superlattices produced by molecular-beam-epitaxy techniques are shown by neutron diffraction to order magnetically in a helix which is incommensurate with the bilayer thickness. One sample consists of 64 bilayers, each bilayer made up of about 15 growth planes (42 Å) of Dy atoms followed by 14 planes (38 Å) of Y atoms. The second sample has 90 layers, each layer consisting of 9 Dy atomic planes and 8 $Dy_{0.5}Y_{0.5}$ alloy planes. The phase coherence of this ordering extends over several bilayers, and is especially striking in the sample where the layers of localized Dy spins are separated by 14 atomic planes of nonmagnetic Y. The fact that the helix chirality propagates across several bilayers rules out a simple scalar Ruderman-Kittel-Kasuya-Yosida coupling between the Dy planes on either side of an Y layer, but suggests instead that a helical spin density wave is induced in the Y conduction electrons. A simple model for the superlattice structure factor demonstrates that observed asymmetries in the magnetic diffraction-peak intensities can be ascribed to the existence of different magnetic modulation wave vectors in each layer type (Dy and Y). In these superlattices the strain clamping by the intervening non-Dy layers and the substrate suppresses the first order ferromagnetic transition found in bulk Dy in both zero and finite fields. Although the planar magnetostriction is clamped, it is observed that the application of a magnetic field in the basal plane produces at low temperatures a second order irreversible transition to a metastable ferromagnetic state. At high temperature the magnetization process is initiated by a reduction of the helical coherence length due to a random-field coupling to the uncompensated Dy layer moment. This allows us to estimate the strength of the interaction through the Y layers.

I. INTRODUCTION

Recent advances in the technologies required to manufacture superlattices and multilayers have not only greatly expanded the control of materials properties, but just as significantly opened new avenues for the investigation of microscopic interactions. For many superlattices interdiffusion can now be limited to be between only two growth planes, so that one has nearly arbitrary control over the stacking sequence of atoms. These sharp chemical boundaries provide an ideal milieu for studies of dimensionality and interface effects, and the control of layer thickness makes it possible to study the details of interactions propagating through the interlayers. The present paper focuses on rare-earth magnetic interactions by studying single-crystal rare-earth-metal superlattices grown by molecular beam epitaxy (MBE).[1,2] We present results principally on a sample consisting of 64 bilayers, each bilayer made up of approximately 15 growth planes (42 Å) of Dy atoms followed by 14 planes (38 Å) of Y atoms. Its designation is then $[Dy_{15} \mid Y_{14}]_{64}$ (sample A). The stacking sequence of the second sample, $[Dy_9 \mid (Dy_{0.5}Y_{0.5})_8]_{90}$ (sample B), is 9 planes of Dy followed by 8 planes of $Dy_{0.5}Y_{0.5}$ alloy.

In bulk dysprosium the localized $4f$ magnetic moments order in an incommensurate helix below a Néel temperature of 179 K with ferromagnetic alignment of the moments in each basal plane and successive planes along the crystallographic c axis rotated by the turn angle ω. Below 85 K the gain in magnetoelastic energy of the ferromagnetic state compared to the helical state[3,4] drives a phase transition to a ferromagnetic state ($\omega=0°$). The helix wavelength increases smoothly from about 25 Å ($\omega=43°$) at the Néel temperature to about 40 Å ($\omega=27°$) just above the first-order collapse to the ferromagnetic state. Yttrium is chemically and structurally very similar to dysprosium but is nonmagnetic (no $4f$ electrons).

Neutron-diffraction measurements show that the superlattice $[Dy_{15} \mid Y_{14}]_{64}$ develops helimagnetic order below about 175 K as in bulk Dy. Remarkably, the phase coherence of this order extends across the 38-Å layers of nonmagnetic Y.[5,6] The measured magnetic correlation range is greater than 370 Å or at least 5 bilayers. Similar observations of long-range magnetic order have been recently obtained in Y-Gd superlattices.[8,7] Helical order also occurs in dilute Y-Gd (Ref. 9) and Y-Tb (Ref. 10) alloy crystals, but at much lower temperatures. We note that to achieve a 40-Å interaction length in dilute alloys would require a concentration below 400 ppm. The present measurements thus provide strong evidence for an incipient conduction-electron spin-density wave in crystalline Y, which is then stabilized by the proximity of local moments.

A separate section of this paper is devoted to the field dependence of the magnetic state in these two multilayers. Those measurements show that the transformation to the field-induced ferromagnetic state is second order, but that

it becomes irreversible at low temperatures where basal-plane anisotropy provides an increased barrier to spin reorientation. At high temperatures the initial magnetization process is accompanied by a reduction of the helix coherence to a single Dy layer as the external field couples to the uncompensated Dy-layer moment in a random-field fashion.

II. SAMPLES AND EXPERIMENTS

The key to the growth of these superlattice structures is the discovery[1] that Y grows epitaxially on a Nb(110) surface, thereby avoiding the reactivity of rare-earth elements with the sapphire substrates. To produce these samples, 1500 Å of Nb was first grown on $(11\bar{2}0)$ sapphire at 1000 °C in an ultrahigh-vacuum MBE chamber (base pressure $\leq 10^{-9}$ torr). About 500 Å of Y and subsequently the Y-Dy samples were grown over a 1-cm^2 area of the Nb(110) at 320 °C at a rate near 0.5 Å/s. The crystallographic c axis of the hexagonal-close-packed rare-earth elements was perpendicular to the growth planes. At room temperature the lattice parameters are $c_Y = 5.740$ Å and $c_{Dy} = 5.655$ Å, while there is about a 2% lattice mismatch in the basal plane. This does not prevent the epitaxial growth of coherent crystalline superlattices. The Y and Dy sources were temperature-controlled effusion cells with computer-controlled shutters. A mass spectrometer monitored the growth rate and reflection high-energy electron-diffraction (RHEED) patterns confirmed the quality of the epitaxial growth. The sample quality, as will be shown in the neutron-diffraction data, is that of a good single crystal with an effective mosaic spread with respect to the crystallographic c axis of about 0.5°.

The number of planes of atoms per bilayer is determined from the neutron diffraction to be 28.3 ± 0.1 for sample A and 17 ± 1 for sample B. Since an absolute calibration of the deposition rates has not been made, it is not surprising that noninteger values are obtained. We also obtain the individual layer thicknesses from the neutron-diffraction data as 14.8 ± 0.2 atomic planes of Dy and 13.5 ± 0.2 atomic planes of Y for sample A. Sample A consisted of 64 bilayers (≈5000 Å), while sample B was 90 bilayers thick (≈4300 Å). The surface areas were 1 cm^2 for sample B and 0.5 cm^2 for sample A, so that the total sample volumes were 0.043 and 0.025 mm^3, respectively.

Neutron-diffraction studies were performed at the National Bureau of Standards Reactor on a standard triple-axis spectrometer. The (002) reflection of pyrolytic graphite (PG) was used to produce a monochromatic incident beam of neutrons at a wavelength of 2.4616 Å (13.5 meV incident energy). A 2-in.-thick PG filter was oriented in the incident beam to remove the higher-order $(00l)$ reflections. A PG(002) analyzer crystal was also employed in the elastic-scattering position after the sample to significantly improve the signal-to-noise ratio. Typically, Soller slit collimators with full-width divergence angles of 40′-25′-25′-40′ were used before the monochromator, sample, analyzer, and detector, respectively, providing instrumental wave-vector resolution along $[000l]$ of $\Delta Q_l = 0.022$ Å^{-1} and transverse resolution of $\Delta Q_t = 0.002$ Å^{-1}. Since the c axis was perpendicular to the growth planes and the magnetic structure is also modulated along the c axis, the neutron-diffraction experiments were preformed in reflection geometry along the $[000l]$ direction. Some scans transverse to $[000l]$ were also performed by rocking the sample with the scattering angle set to an observed $[000l]$ peak to measure the effective sample mosaic widths.

For the zero-field experiments the samples were thermally anchored with vacuum grease to an aluminum plate and then mounted on the cold finger of a controlled-flow cryostat. The temperature could then be regulated between 300 K and 5 K with a precision of 0.1 K. Care has been taken to align the samples using the superlattice Bragg peaks instead of the much stronger substrate peaks, since the registry between the substrate and the superlattice may not be perfect. Field-dependent studies were performed by similarly mounting the samples in a cryostat which was then lowered into a Nb-Ti split-vertical-coil superconducting magnet where the field in the basal plane could be varied from 0 to 70 kOe.

III. SUPERLATTICE STRUCTURE-FACTOR CALCULATION

A. Lattice and magnetic phase mismatch

It is usually the case that corrections for absorption, extinction, and scattering geometry (Lorentz factor) must be considered when translating observed Bragg-peak intensities into values for the structure factor. However, as shown by Bacon,[11] for crystals on the order of 1000 Å thick the reflectivity of neutrons is typically on the order of 1%, so that extinction will be negligible. Also, the linear absorption coefficient for 2.5-Å neutrons in Dy is 45 cm^{-1}, so that the absorption of neutrons passing through 2500 Å of Dy is only 0.1%. Under these conditions it is well known[12,13] that the intensity obtained by integrating a longitudinal wave-vector scan through a given Bragg reflection is proportional to $F^2(Q)/\sin\theta$, where the quantity $F^2(Q)$ is the structure factor for the reflection and $\sin\theta$ is the appropriate Lorentz factor in the case that the sample is fully bathed in the incident beam (2θ is the scattering angle). When the mosaic of the sample crystal is large compared to the instrumental resolution there are additional small corrections[12] which are again straightforward.

We shall calculate the superlattice structure factor beginning from the differential neutron cross section with nuclear and magnetic terms:

$$\frac{d\sigma}{d\Omega}(\mathbf{Q}) = \left[\sum_r \exp(i\mathbf{Q}\cdot\mathbf{r})b_r\right]^2 + \left[\sum_r \exp(i\mathbf{Q}\cdot\mathbf{r})\mathbf{p}_r\right]^2 . \tag{1}$$

The vectors $\mathbf{r}$ denote the positions of the atoms in the crystal, while b_r is the nuclear-scattering amplitude of that atom. When the magnetic moments are perpendicular to $\mathbf{Q}$, as in the present experiments, the effective magnetic scattering amplitude can be expressed as $\mathbf{p}_r = \sigma_m f_r(Q)\mathbf{S}_r$, where $\sigma_m = 0.2695\times10^{-12}$ cm and

$f_r(Q)$ is the magnetic form factor for the moment $\mathbf{S}_r$ (in Bohr magnetons) at site $\mathbf{r}$.

In this paper we are only interested in the scattering along the [000l] direction, so that the calculation of the cross section can be restricted to one dimension (with a possible configurational average across the basal plane). Then with only the assumption that the bilayer thickness (L) is uniform, the atom positions along the c axis can be expressed as $r(m,n)=mL+z(n)$, where m indexes the bilayer in which the atom resides and $z(n)$ is the relative position along the c axis of the nth atom within the bilayer. Thus $z(N_L)=L$ for a bilayer of N_L atomic planes. Since the nuclear amplitudes have the periodicity of the bilayer, the nuclear part of the cross-section factors as

$$\left[\frac{d\sigma}{d\Omega}(Q)\right]_{\text{nuc}} \propto S_{\text{nuc}}(Q) = \left[\sum_m e^{imQL}\right]^2 \left[\sum_n e^{iQz(n)}b_n\right]^2 . \quad (2)$$

The first factor corresponds to the usual Bragg δ function, producing peaks at the bilayer reciprocal-lattice vectors $Q=\tau_{\text{nuc}}=l(2\pi/L)$ for integer l with peak full widths at half maxima (FWHM's) of approximately $2\pi/(NL)$, where N is the number of bilayers which scatter coherently (N is less than or equal to the total number of bilayers in the sample). The second factor is the nuclear structure factor $F^2_{\text{nuc}}(Q)$ for the bilayer unit cell.

In the case of the magnetic scattering, the effective magnetic scattering amplitudes do not necessarily have the periodicity of the bilayer (incommensurability). Those amplitudes can quite generally be expressed as

$$\mathbf{p}(m,n)=p_n\{\hat{\mathbf{x}}\cos[m\Phi+\phi(n)]\pm\hat{\mathbf{y}}\sin[m\Phi+\phi(n)]\} . \quad (3)$$

In this notation the total phase shift of the helix across each bilayer is Φ and the phase shift at site n with respect to the start of each bilayer is $\phi(n)$, so that $\Phi=\phi(N_L)$. Since the magnitudes p_n of the effective magnetic scattering amplitudes do have the periodicity of the bilayer, the magnetic part of the cross section splits into two terms:

$$\left[\frac{d\sigma}{d\Omega}(Q)\right]_{\text{mag}} \propto S_{\text{mag}}(Q)+S_{\text{mag}}(-Q) , \quad (4)$$

where the magnetic scattering function is

$$S_{\text{mag}}(Q)=\tfrac{1}{2}\left[\sum_m e^{im(QL+\Phi)}\right]^2 \left[\sum_n e^{i(Qz(n)+\phi(n))}p_n\right]^2 . \quad (5)$$

The magnetic Bragg peaks are located at $Q=\tau_{\text{nuc}}-\Phi/L$ and $Q=\tau_{\text{nuc}}+\Phi/L$ for $S_{\text{mag}}(Q)$ and $S_{\text{mag}}(-Q)$, respectively [recall that $\tau_{\text{nuc}}=l(2\pi/L)$]. Thus these two sets of magnetic peaks are separated from each other by $2\Phi/L$. Since QL in Eq. (2) is replaced by $QL+\Phi$ in Eq. (5), the FWHM of the magnetic Bragg peaks must be greater than the FWHM of the nuclear Bragg peaks. That is, the magnetic coherence length is limited by the phase coherence as well as the chemical coherence. The second factors in $S_{\text{mag}}(Q)$ and $S_{\text{mag}}(-Q)$ are the respective magnetic structure factors, $F^2_{\text{mag}}(Q)$ and $F^2_{\text{mag}}(-Q)$. Note that these results are only dependent on Φ modulo 2π.

In order to calculate the structure factors, we shall initially assume sharp interfaces and uniform layers for the superlattice. That is, we have rectangle-wave modulation of the constituent concentrations, lattice spacings, and magnetic phase shifts. The postulates of the model are illustrated in Fig. 1. The N coherent bilayers of the sample each consist of A and B layers, which, in turn, are made up of N_A and N_B atomic planes, respectively, with $N_A+N_B=N_L$. The atomic planes in A and B are separated by d spacings d_A and d_B. The coherent nuclear scattering amplitudes are b_A and b_B. The magnetic moments are S_A and S_B. We also allow for the possibility that the magnetic phase shifts between atomic planes are different in the two layers by defining separate magnetic modulation wave vectors κ_A and κ_B.

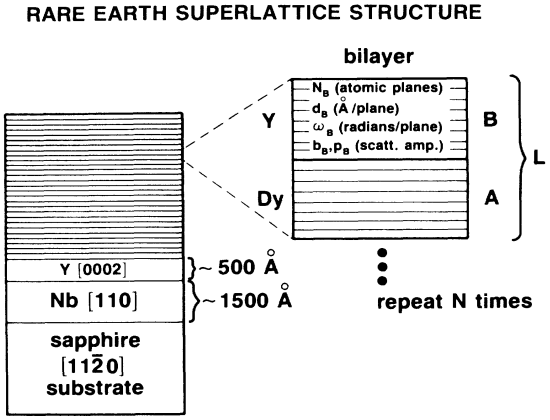

FIG. 1. A schematic of rare-earth-metal superlattices is shown, introducing the notation used in the text. Each bilayer consists of N_A atomic planes of type-A (e.g., DY) atoms and N_B atomic planes of type-B (e.g., Y) atoms. The rectangle-wave modulated interplanar spacings and turn angles are d_A, d_B, ω_A, and ω_B. The total bilayer thickness is L.

To illustrate the main features, we can assume the extreme contrast case where the B-layer scattering amplitudes (b_B and p_B) are zero, but allow the magnetic wave vectors $\kappa_A\neq\kappa_B$. In a given bilayer the atoms which contribute to the observed scattering are positioned along the c axis at $z(n)=nd_A$, where $n=[0, N_A-1]$. The relevant magnetic phase shifts also index as $\phi(n)=n\kappa_A d_A$, with the total bilayer phase shift given by $\Phi=N_A\kappa_A d_A+N_B\kappa_B d_B$. In this simple rectangle-wave model the scattering functions can be written in closed form[14] as

$$S_{\text{nuc}}(Q)=\frac{\sin^2(NQL/2)}{\sin^2(QL/2)}\frac{\sin^2(N_AQd_A/2)}{\sin^2(Qd_A/2)}b_A^2 \quad (6)$$

and

$$S_{\text{mag}}(Q)=\frac{\sin^2[N(QL+\Phi)/2]}{\sin^2[(QL+\Phi)/2]}\times\frac{\sin^2[N_A(Q+\kappa_A)d_A/2]}{\sin^2[(Q+\kappa_A)d_A/2]}\tfrac{1}{2}p_A^2 . \quad (7)$$

We have not written out $S_{\text{mag}}(-Q)$ since it is identical to Eq. (7) with Q replaced by $-Q$. The first factors in Eqs. (6) and (7) are the Bragg terms discussed previously, and

the second factors are the unit-cell structure factors $F^2(Q)$. $F^2_{\rm nuc}(Q)$, $F^2_{\rm mag}(Q)$, and $F^2_{\rm mag}(-Q)$ have peaks at $Q=l(2\pi/d_A)$, $l(2\pi/d_A)-\kappa_A$, and $l(2\pi/d_A)+\kappa_A$, respectively, for integer l. The FWHM of these peaks is approximately $2\pi/(N_A d_A)$, so that $L/(N_A d_A)+1$ of the nearby superlattice Bragg peaks will have a considerable intensity (see Fig. 2).

Provided that the coherence length of the superlattice is much larger than a single layer thickness, the superlattice Bragg peaks will be much narrower than the structure-factor peaks. Thus the observed intensity maxima will be at the Bragg positions with integrated intensities proportional to the product of the structure factor evaluated at the Bragg positions and the corresponding Lorentz factor.

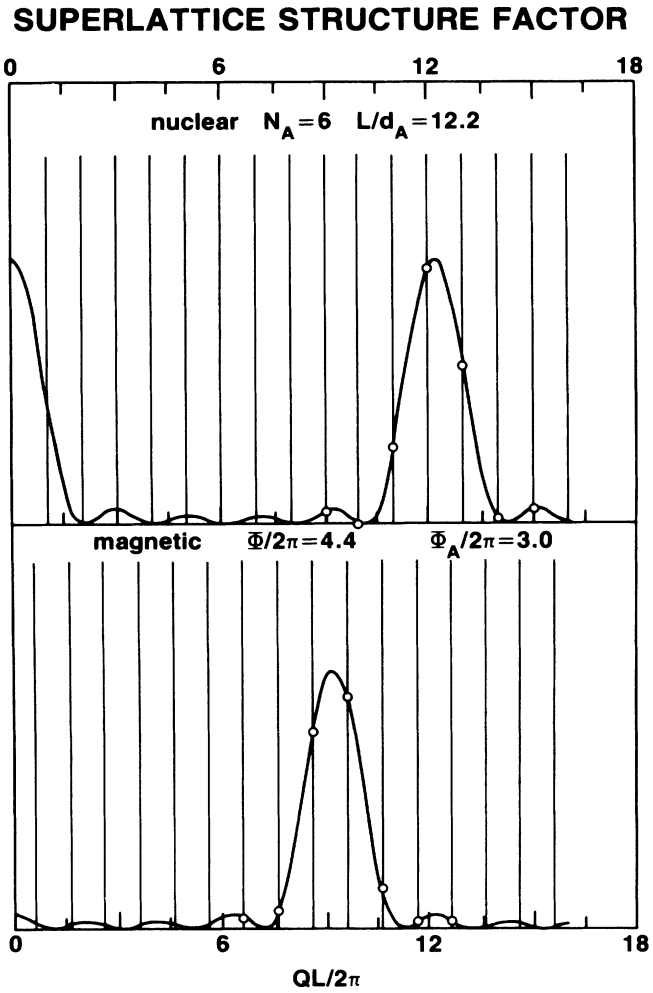

FIG. 2. A visualization of the superlattice structure factors. The sharp spikes are the superlattice Bragg peaks spaced at intervals of $2\pi/L$, while the curve defines the structure-factor envelope. The calculated values of the structure factor are obtained at the intersection of the envelope with the Bragg peaks. Lattice mismatch shifts the peak of the envelope function away from a Bragg position, resulting in asymmetry of the superlattice satellite intensities. Note that the relationship of the magnetic Bragg peaks to the magnetic structure-factor envelope is different from the nuclear case. This results in a different asymmetry of the magnetic satellite intensities.

This simple model demonstrates that lattice mismatch along the c axis (L/d_A is not an integer) causes the structure factor to peak at a Q different from any superlattice Bragg peak position, which results in the asymmetry of the observed intensities.[14] This is illustrated in Fig. 2. Note that the intensity asymmetry for the $S(Q)$ and $S(-Q)$ groups of magnetic peaks are, in general, different unless the total bilayer phase shift satisfies $\Phi=\kappa_A L$ modulo 2π (or, equivalently, $\kappa_A=\kappa_B$ modulo $2\pi/L$). If $\Phi=\kappa_A L$, the two groups of peaks are simply shifted along the Q axis from one another by $2\kappa_A$.

Provided that the lattice mismatch is sufficiently small, we can obtain the number of atomic planes per bilayer from the position of the most intense nuclear Bragg peak. If we assume an integer number of atomic planes per bilayer then the primary Bragg peak position is given by $l(2\pi/L)$, where l is an integer. For small lattice mismatch this must be near the peak in the nuclear structure factor, which we write as $2\pi/\langle d\rangle$. It is easy to show that the structure factor peaks at a position which corresponds to a weighted average of the d spacings in layers A and B. Thus $\langle d\rangle$ is between d_A and d_B and is given to a good approximation by $\langle d\rangle=L/N_L$. Since l and N_L must be integers, this immediately implies that $l=N_L$ and $\tau_0=N_L(2\pi/L)$. A similar argument using an extended unit cell shows that this remains true when N_L is noninteger.

B. Effects of imperfect rectangle-wave modulation

At this point we consider modifications to the above model in order that we might make reliable inferences from our data analysis. In particular, perfect rectangle-wave concentration modulation is removed in a real superlattice by diffusion and island formation at the interface during the crystal-growth process (HEED measurements suggest that island formation is minimal in the present superlattices). Even without diffusion the d spacings are expected to modulate smoothly,[15,16] and without diffusion or strain modulation the band structures might still be expected to obtain some gradual transition from one layer to the next. We cannot measure the infinite number of Fourier components necessary to extract directly the real-space modulation functions, so we resort to a model for the interface. The simplest way to include these imperfections is to write the rectangle wave in terms of its Fourier components and to include a damping factor. Thus we write the concentration modulation for layer-A atoms as a diffusion-equation solution (with α equivalent to a time variable),

$$c_A(n,\alpha)=\frac{N_A}{N_L}+\frac{1}{\pi}\sum_{m=1}^{\infty}e^{-\alpha m^2}\frac{1}{m}\left[\sin\left[\frac{2\pi m}{N_L}(n-\tfrac{1}{2})\right]-\sin\left[\frac{2\pi m}{N_L}(n-\tfrac{1}{2}-N_A)\right]\right]. \quad (8)$$

The rectangle wave corresponds to a value of zero for the parameter α, and as α approaches infinity complete diffusion is reached. This choice of parametrization has the recommending features of preserving the superlattice periodicity and conserving the number of atoms of each layer type. Note that here n is a site index, so that the interfaces correspond to values of $\frac{1}{2}$ and $\frac{1}{2}+N_A$. This form of the concentration modulation allows us to write the effective coherent scattering amplitude at each unit cell site as

$$b_n = c_A(n) b_A + [1 - c_A(n)] b_B \ . \tag{9}$$

This expression can easily be generalized to the case that there are binary alloys in each layer, and an identical expression can be obtained for the p_n (replacing b by p everywhere). In an analogous fashion, we write the d-spacing modulation as

$$d(i,\beta) = \frac{L}{N_L} + \frac{1}{\pi}(d_A - d_B) \times \sum_{m=1}^{\infty} e^{-\beta m^2} \frac{1}{m} \left[\sin\left(\frac{2\pi m i}{N_L} \right) - \sin\left[\frac{2\pi m}{N_L}(i - N_A) \right] \right] , \tag{10}$$

and the magnetic phase shift per atomic plane as

$$\omega(i,\gamma) = \frac{\Phi}{N_L} + \frac{1}{\pi}(\omega_A - \omega_B) \times \sum_{m=1}^{\infty} e^{-\gamma m^2} \frac{1}{m} \left[\sin\left(\frac{2\pi m i}{N_L} \right) - \sin\left[\frac{2\pi m}{N_L}(i - N_A) \right] \right] . \tag{11}$$

In Eqs. (10) and (11), i is an interval index with the interfaces centered at intervals numbered zero and N_A. Note that again these expressions have the superlattice periodicity, and for all values of the modulation parameters β and γ the bilayer thickness and total phase shift across the bilayer are conserved. Obviously d_A, d_B, ω_A, and ω_B are the d spacings and turn angles in the case of rectangle-wave modulation. The generalized expressions for the unit-cell atom positions and phase shifts are then

$$z(n,\beta) = \sum_{i=0}^{n-1} d(i,\beta) \quad \text{with } z(N_L,\beta) = L \tag{12}$$

and

$$\phi(n,\gamma) = \sum_{i=0}^{n-1} \omega(i,\gamma) \quad \text{with } \phi(N_L,\gamma) = \Phi \ . \tag{13}$$

Alternatively, one could define a magnetic wave vector on each interval equivalent to $\kappa(i) = \omega(i)/d(i)$. The present parametrization is simpler, however, since the total phase shift Φ is determined only by the observed magnetic peak positions and not their intensities. A representation in which Φ is conserved is then ideal for our purposes.

The above formalism can be extended readily to superlattices with noninteger numbers of atomic planes by simply extending the unit cell for the structure-factor calculation an integer number of times until the total number of planes is an integer (e.g., the multiplicative factor is 6 for sample A, since 6×28.33 and 6×13.5 are nearly integers). This extension retains the conservation of total bilayer phase shift and bilayer thickness. Note, however, that noninteger Bragg indices must be used.

In summary, these calculations show that observed peak positions will determine the bilayer thickness L, the total magnetic phase shift across the bilayer, Φ, and the total number of atomic planes per bilayer. The remaining parameters which can be determined by the relative peak intensities are $d_{AB} = d_A - d_B$, $\omega_{AB} = \omega_A - \omega_B$, the sizes of the magnetic moments, and the modulation parameters α, β, and γ. The relative intensities of the main nuclear peak and its satellites are dominated by d_{AB}, while the relative magnetic peak intensities are likewise most sensitive to ω_{AB}. The modulation parameter which will have the most significant effect on the results of the data analysis is α (concentration). Since the number of atoms is conserved, the effect of diffusion is to reduce the satellite intensities while leaving the primary peaks unchanged (the width of the structure-factor envelope decreases). The satellite intensities are thus converted into incoherent scattering.

IV. ZERO-FIELD DIFFRACTION

A. Nuclear intensities and coherence range

The [000l] scans for samples A and B are shown in Figs. 3(a) and 3(b), respectively, for a range of temperatures. The most prominent feature in the data is the approximately temperature-independent primary nuclear Bragg peak (τ_0) at a wave-vector transfer (Q) of about 2.22 Å^{-1}. A second nuclear Bragg peak at a slightly higher Q appeared in some of the scans for sample A, and has been subtracted from the data producing the enlarged error bars observed in the figure. This second peak is not due to the sample and is tentatively identified with the Y substrate layer or some other rare-earth impurity phase.[5] It appears in the data at a Q value about 3% higher than expected for bulk Y. The intensity of this peak is ostensibly a function of the crystal-orientation procedure on the spectrometer (and/or time). In fact, in one of the data sets this peak is entirely absent. A similarly positioned though much less intense peak is found in sample B, where it has not been subtracted since it does not obscure any other relevant peaks.

It is possible to obtain considerable information from the raw data before proceeding to a detailed analysis of the peak intensities. The peak positions and widths alone are sufficient to obtain the bilayer thickness (L), the total magnetic phase shift across the bilayer (Φ), the number of atomic planes per bilayer (N_L), and the nuclear and magnetic coherence lengths. The nuclear coherence length along the superlattice growth direction (c axis) is deter-

mined from the intrinsic width of the primary nuclear Bragg peak. Using 40′-25′-25′-40′ collimators the instrumental Gaussian FWHM at the nuclear Bragg position is $\Delta Q_l = 0.022$ Å^{-1} (independent of any sample mosaic because of the symmetric collimators). This value is confirmed by measuring the instrumentally limited width of the sapphire [11$\bar{2}$0] peak in the same scan. Fitting the observed Bragg peak gives a Gaussian FWHM of $\Delta Q_l = 0.0250$ Å^{-1} (for both samples), so that the deconvoluted intrinsic linewidth is $\Delta Q_l = 0.015$ Å^{-1}. Following Scherrer,[17] the correlation range or crystallite width is then approximately $2\pi/\Delta Q_l = 420$ Å.

As our model calculation in Sec. III shows, there should exist a series of nuclear satellites of the main Bragg peak at Q intervals of $2\pi/L$. The nuclear satellite at higher Q (2.3 Å^{-1}) than the primary Bragg peak is clearly visible in sample A, although the corresponding satellite at lower Q (2.14 Å^{-1}) cannot be easily distinguished. This strong asymmetry of the nuclear satellite intensities is also observed in earlier x-ray-diffraction data[2] for this sample, and, as our model calculation in Sec. III shows, is a consequence of the lattice mismatch along the c axis between the Dy and Y layers. The nuclear-scattering -amplitude contrast is not great enough in sample B, where the layers are Dy and $Dy_{0.5}Y_{0.5}$ ($b_{Dy} = 1.71$ and $b_Y = 0.775$ in units of 10^{-12}cm), to make the satellites visible in the diffraction scan.

As we have remarked above, when the lattice mismatch is reasonably small, the position of the primary nuclear Bragg peak is $\tau_0 = N_L(2\pi/L)$. Dividing τ_0 by the satellite separation then yields N_L. For example, at 80 K in sample A we obtain $\tau_0 = 2.217$ A^{-1} and $2\pi/L = 0.0784 \pm 0.0003$ Å^{-1}, so that $N_L = 28.2$. We have repeated this calculation for all the sample-A data to obtain an average of 28.3 ± 0.1 atomic planes. The difficulty of observing superlattice-modulation peaks for sample B prevents such an accurate determination (except in the field-induced remanent state described below). The determination of individual layer thicknesses is described in the field-dependence section below. Note that it is quite reasonable to obtain noninteger numbers of atomic planes per bilayer, since the shuttering is controlled by the amount of each element deposited rather than the completion of the individual epilayers.

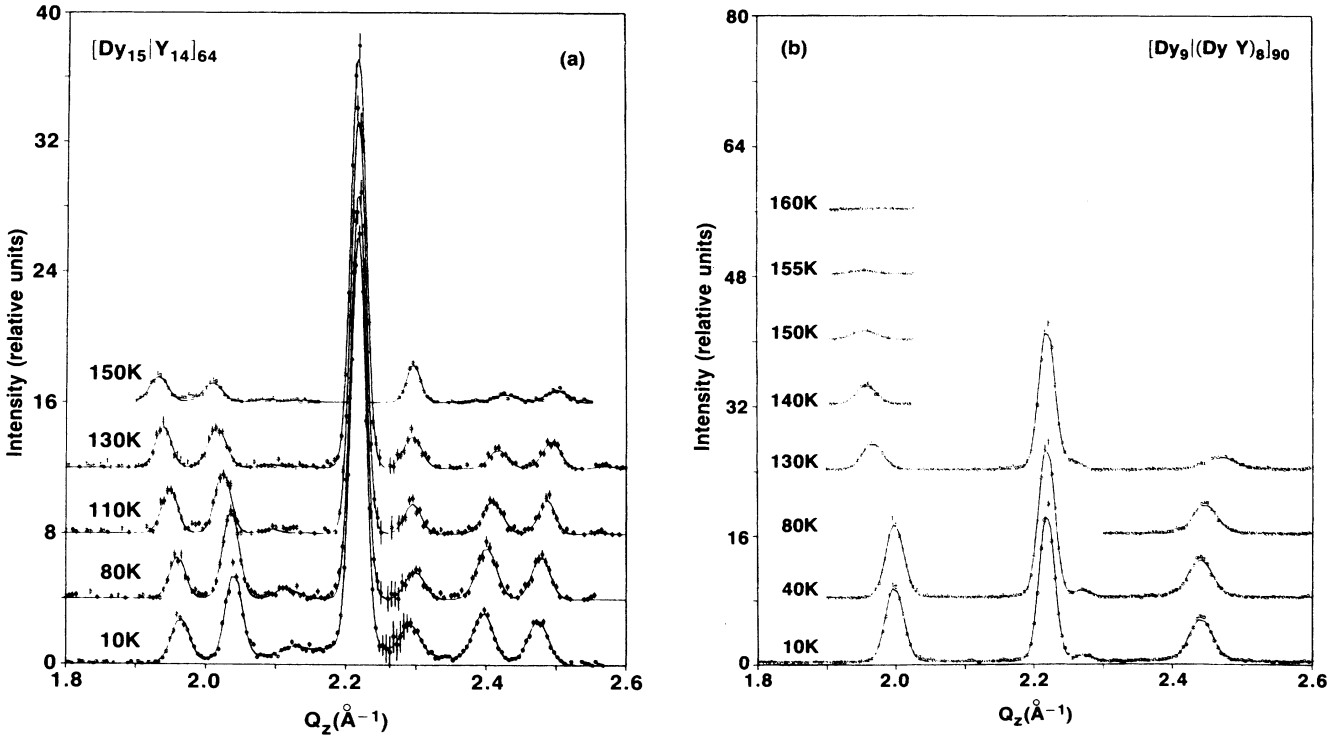

FIG. 3. The [000l] scans are shown for samples A and B in zero field. The curves through the data are Gaussian fits from which the superlattice structure factors are derived. The magnetic satellite intensity increases with decreasing temperature and the peak positions move toward the primary nuclear Bragg peak (0002) = 2.22 Å^{-1}. This is the same behavior found in the helimagnetic phase of bulk Dy, although no long-range ferromagnetism is observed in the superlattices down to 10 K. In sample A the first peak at higher Q from the (0002) is the first-order nuclear satellite deriving from the superlattice modulation of the nuclear scattering amplitude. Superlattice modulation of the helimagnetic satellites is also observed in sample A, indicating magnetic phase coherence through the magnetically "dead" yttrium layers across about four bilayers. The peak intensities are controlled by lattice and magnetic phase mismatch in the separate layers as described in the text.

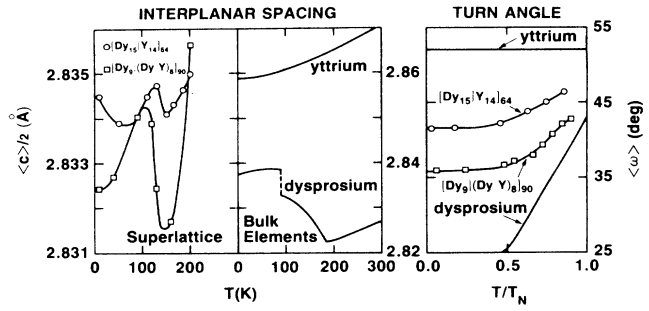

FIG. 4. The average interplanar spacings along the c axis are obtained from the position of the primary nuclear Bragg peak. The temperature dependence in the superlattice is a weighted average of the behavior in the constituent materials. Note the change of scale when comparing to the bulk materials. Also shown is the average turn angle in the superlattices as well as in the bulk materials. Again, an average of the bulk values is obtained.

Since the number of planes per bilayer is fixed, the temperature dependence of the bilayer thickness (L) can be precisely determined from the temperature dependence of τ_0. The values of the average spacing, L/N_L, of the atomic planes along the c axis are plotted in Fig. 4 versus the temperature for samples A and B. When compared with the temperature dependence of interplanar spacings in bulk Dy and Y in the same figure, it is seen that the superlattice behavior is an average of its bulk constituents. The expansion along the c axis below T_N is clearly characteristic of the unforced magnetostriction in Dy.[18] Note that the orthorhombic distortion which occurs in bulk Dy at the ferromagnetic transition will be clamped by the superlattice Y layers and the substrate, although the c axis magnetostriction can occur. The determination of separate values of the lattice parameters in each individual layer will be made in the detailed data analysis below.

B. Magnetic intensities and coherence range

As the temperature is lowered, additional peaks of magnetic origin appear on either side of τ_0 as shown in Fig. 3. In sample B only two additional peaks are found in the zone about the primary nuclear peak and thus the scattering pattern is identical to that found in a conventional helimagnetic phase such as bulk Dy. In sample A, by contrast, a triad of magnetic peaks appears on either side of τ_0 below 175 K (e.g., positioned at $Q=1.96$, 2.04, and 2.12 Å^{-1} at 10 K). As in the case of the nuclear scattering, the magnetic-scattering-amplitude contrast in sample B is considerably weaker than in sample A. This is the main reason for the disparity in the diffraction patterns of the two samples, although, as we will discuss later, small amounts of interdiffusion likely contribute to this effect also.

Although the individual magnetic peak intensities are determined by the magnetic phase shifts as well as the magnitudes of the magnetic moments, we can estimate the ordering temperatures for sample A by computing the integrated magnetic intensity in the Brillouin zone about τ_0. We treat the 200-K scan as a nonmagnetic background and subtract it from the lower-temperature scans. The resulting counts are summed over the scan and weighted by the free-ion form factor of Dy and the appropriate Lorentz factor. The results are plotted as a function of temperature in Fig. 5. Assuming that in their equilibrium configuration the magnetic moments lie in the basal plane, the integrated magnetic intensities (assumed to be the result of elastic scattering) are then proportional to the configurationally averaged moment squared (including the form factor). Although the exact power-law dependence of the order parameter on temperature is not known (especially for these superlattices, which have a considerable effective magnetic surface area compared to their volume), it is clear that a straight line can be drawn through our integrated intensities in Fig. 5 as T_N is approached (corresponding to a mean-field magnetization critical exponent of $\frac{1}{2}$) to obtain an approximate ordering temperature T_N (sample A)$\approx 176\pm 1$ K, which may be compared to the value of 165 K determined by superconducting quantum-interference device (SQUID) magnetometry in an applied field of 2 kOe. The curve through the data in Fig. 5. is a fit to the $J=\frac{15}{2}$ Brillouin function for the spontaneous magnetization, showing that the configurationally averaged (and thermally averaged) Dy moment has a conventional temperature dependence. In sample B there are only single magnetic satellites, so that the temperature dependence of the square of the order parameter is obtained directly by plotting the individual peak intensities as shown in Fig. 5. The ordering temperature thus obtained is T_N (sample B)$\approx 163\pm 1$ K.

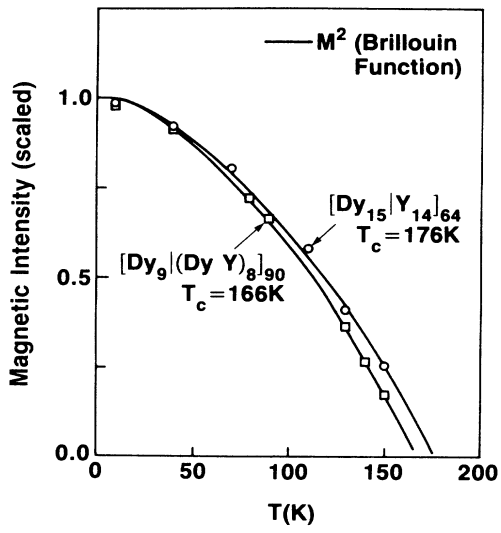

FIG. 5. Relative integrated magnetic intensity for samples A and B vs the temperature, giving ordering temperatures of 176 K for sample A and 163 K for sample B. The solid lines are fits to the $J=\frac{15}{2}$ Brillouin function, showing that conventional behavior is obtained.

The interlayer coupling in sample A is weak (as will be shown), so that the ordering temperature is predominantly determined by the average exchange energy in the Dy layer. Finite-size effects on this average exchange have been investigated by Kwo *et al.*[7] in Gd-Y superlattices. Since the Néel temperature for $Dy_{0.5}Y_{0.5}$ is about 115 K,[19] the interlayer coupling in sample B will be weaker than the intralayer Dy coupling. Again, T_N will be determined primarily by the Dy-layer average exchange. This offers a reasonable explanation for the proximity of T_N in samples A and B and bulk Dy. The dependence of T_N on the Y-layer thickness is also presently under investigation.

The magnetic coherence length is less precisely determined than the nuclear coherence length, since, as we mentioned previously, the magnetic peak width depends on the regularity of both L and Φ. We have fitted the most intense magnetic peaks to Gaussians and performed the same deconvolution as in the case of the nuclear peaks to obtain a lower bound of 370 Å for the magnetic phase coherence length in sample A and 300 Å in sample B. The magnetic peak widths are independent of temperature below T_N in sample A, indicating a well-defined phase transition. However, in sample B the widths increase at temperatures above about 130 K (recall that $T_N \approx 115$ K for $Dy_{0.5}Y_{0.5}$).

The asymmetries displayed in the magnetic superlattice peaks for sample A result from a combination of lattice mismatch (asymmetry within the group of peaks on a given side of τ_0) and magnetic wave-vector mismatch ($\kappa_A \neq \kappa_B$ producing asymmetry between the groups of peaks on either side of τ_0). This asymmetry and its strong temperature dependence permits us to obtain detailed information on the magnetic wave vectors, as we show below.

With decreasing temperature the magnetic peak positions move in towards τ_0 in both samples. This behavior is characteristic of bulk Dy, where the wavelength of the magnetic modulation increases as the ferromagnetic transition is approached, and is a consequence of the opening of superzone gaps at the Fermi surface in the presence of local moments.[20] Note that no additional intensity is observed at the nuclear peaks down to 10 K, indicating that a transition to long-range ferromagnetic order is absent (although we shall demonstrate the presence of a broad ferromagnetic background which does increase at low temperature).

Drawing once again upon our model calculation, we can determine the total magnetic phase shift (Φ modulo 2π) across the bilayer from the positions of the magnetic peaks. Recall from Eq. (5) that the magnetic Bragg peaks are located at $Q=\tau_{\rm nuc}\pm\Phi/L$. We have thus obtained Φ as a function of temperature for both samples, and these values are plotted in Fig. 4 as $\langle\omega\rangle=\Phi/N_L$ representing the average turn angle for the bilayer. For comparision, the turn angles in bulk Dy and Y are also shown with the value for Y obtained from the dilute rare-earth alloys.[21] Clearly, $\langle\omega\rangle$ is quite different from the turn angle in bulk Dy. The individual phase shifts in each layer will be more significant as shown below, although as with the values of L, the values of Φ are necessary in order to fit the peak intensities and extract additional information.

C. Turn angles and magnetic moments

We proceed by extracting the structure factors for the observed peaks. These values are used in a least-squares fit to obtain d_A, d_B, ω_A, and ω_B. We have been careful to scan the Bragg peaks in the transverse direction to ensure that we obtain the full integrated intensity. The effective mosaic widths ($\eta=\Delta Q_t/Q$) are listed in Table II. For the magnetic peaks these are nearly independent of Q, as would be the case for a true mosaic distribution of crystallite orientations. However, the mosaic width for τ_0 has an effective mosaic which is smaller than the mosaic widths for the superlattice satellites. We can calculate the scattering function for a transverse scan through a nuclear peak by writing $\mathbf{Q}=(N_L+k)\mathbf{c}^*+\xi\mathbf{a}^*$ and the atomic positions as $\mathbf{R}=[m+z(n)/L]\mathbf{c}+l\mathbf{a}$. The k, l, m, and n are integers, $|\mathbf{c}|=2\pi/L$, and $\mathbf{a}$ and $\mathbf{a}^*$ are the direct and reciprocal-lattice vectors in the basal plane. Note that $k=0$ corresponds to the transverse scan through τ_0. Then, the scattering function is

$$S(k,\xi)=\left|\sum_{l,m,n}\exp(i\mathbf{Q}\cdot\mathbf{R})b(lmn)\right|^2 = \left|\sum_{l}\exp(2\pi i\xi l)f(k,l)\right|^2 , \tag{14}$$

with

$$f(k,l)=\sum_{m,n}\exp(2\pi ik/L)b(lmn) . \tag{15}$$

When $k=0$ the function $f(k,l)$ should be nearly independent of l, since $b(lmn)$ is averaged over the entire coherent length along the c axis. It is clear that $f(k,l)$ becomes sensitive to the interface roughness when $k\neq 0$, so that $S(k\neq 0,\xi)$ measures the transverse coherence length along the interface. This explains why τ_0 is the sharpest peak in the transverse scans.

Table II gives the effective Lorentz factors obtained from the peak positions and the measured effective sample mosaic widths. The structure factor given is the integrated longitudinal intensity divided by the Lorentz factor. We have least-squares-fitted the values of $|F(Q)|^2$ to our model for the superlattice structure factors, Eqs. (2) and (5), using Eqs. (8)–(11), with the predetermined values of L, Φ, N_L, and N_A, and the modulation parameters α, β, and γ held fixed (there is insufficient contrast to perform this analysis for sample B). The values of the modulation parameters were determined from an initial pass through the data which showed that $\alpha=0.1\pm0.03$ and $\beta\approx\gamma\approx\alpha$. The concentration modulation resulting from $\alpha=0.1$ is plotted in Fig. 6, showing that the interface width (due to diffusion, variation of L, or island formation) is about 4–5 atomic planes.

The results for the individual layer lattice parameters and turn angles in sample A are plotted in Fig. 7. Note from Eqs. (10) and (11) that these are the effective rectangle-wave values, and are thus representative of the central regions of the layers. Also shown are the total phase shifts from atomic plane 1 to atomic plane N_A ($\Phi_{\rm Dy}$ across the Dy layer) and from atomic plane N_A to atomic plane N_L+1 ($\Phi_{\rm Y}$ from Dy plane to Dy plane through the Y layer). In Fig. 8 we show the temperature dependence

TABLE I. Structure factors for $[Dy_{15}|Y_{14}]$.

T (K)		Q (Å^{-1})	Lorentz factor	$\|F(Q)\|^2_{meas}$	$\|F(Q)\|^2_{calc}$
5	mag −				
		1.9645	1.095	15.87±0.87	16.19
		2.0396	1.049	25.46±1.45	25.90
		2.1147	1.006	4.33±0.8	4.67
	mag +				
		2.3964	0.880	20.01±1.71	19.01
		2.4747	0.830	21.58±1.20	20.99
		2.5529	0.799	1.40±0.58	0.58
	nuc	2.1379	0.836	1.48±1.34	1.38
		2.2167	1.029	100.00±3.38	100.06
		2.2956	0.776	10.19±2.45	9.83
10	mag −	1.8871	1.135	0.63±0.22	0.03
		1.9635	1.082	14.02±0.82	13.94
		2.0399	1.036	26.70±1.64	27.11
	mag +				
		2.3965	0.869	20.81±2.24	18.79
		2.4740	0.819	20.66±1.64	21.59
		2.5516	0.790	1.23±0.34	1.27
	nuc	2.1395	0.825	1.42±1.12	0.67
		2.2168	1.016	100.00±4.85	100.45
		2.2923	0.767	14.24±3.36	12.79
80	mag −				
		1.9590	1.098	17.98±1.26	16.75
		2.0360	1.051	27.14±1.44	28.17
		2.1130	1.007	5.93±0.54	5.36
	mag +	2.3208	0.910	0.72±0.72	1.98
		2.3997	0.879	22.81±2.01	22.81
		2.4787	0.828	19.27±1.62	20.65
	nuc	2.1387	0.836	2.30±0.54	1.82
		2.2172	1.029	100.00±2.70	100.45
		2.2957	0.776	13.64±3.77	8.90
110	mag −	1.8716	1.145	0.70±0.35	0.07
		1.9478	1.091	12.97±2.09	13.32
		2.0244	1.044	17.46±2.43	18.82
	mag +				
		2.4087	0.864	15.37±2.33	12.94
		2.4865	0.815	14.61±2.26	16.76
		2.5647	0.785	1.84±0.49	1.29
	nuc	2.1387	0.825	1.67±0.52	1.25
		2.2167	1.016	100.00±4.28	100.90
		2.2939	0.766	12.17±2.43	10.61
130	mag −				
		1.9392	1.110	12.28±0.83	11.15
		2.0186	1.060	12.80±0.86	14.28
		2.0980	1.014	2.49±0.27	1.93
	mag +				
		2.4151	0.873	9.62±1.08	8.64
		2.4947	0.823	12.74±1.05	14.07
		2.5743	0.783	2.98±0.60	1.79
	nuc	2.1382	0.836	1.23±0.36	0.83
		2.2167	1.029	100.00±1.91	100.36

TABLE I. (*Continued*).

T (K)		Q (Å^{-1})	Lorentz factor	$\lvert F(Q)\rvert^2_{\text{meas}}$	$\lvert F(Q)\rvert^2_{\text{calc}}$
		2.2950	0.776	13.11±1.43	12.16
150	mag −				
		1.9314	1.114	8.02±0.57	7.20
		2.0098	1.065	6.57±0.56	6.82
		2.0882	1.019	1.48±0.59	0.56
	mag +				
		2.4250	0.869	4.67±0.67	3.82
		2.5034	0.819	6.57±0.70	7.98
		2.5818	0.781	1.85±0.24	1.45
	nuc	2.1386	0.836	1.19±0.36	1.00
		2.2172	1.028	100.00±1.62	100.38
		2.2956	0.776	12.71±1.07	11.40

of the Dy thermal average moment determined from the fits and the resulting magnitude of the uncompensated (net) Dy-layer moment, given analytically by the sum of the Dy-moment vectors along the c axis in a single Dy layer,

$$\mu_{\text{net}}(m)=\sum_{n=1}^{N_A}\mathbf{S}(m,n)\ , \tag{16}$$

with

$$|\mu_{\text{net}}(m)|=\mu_{\text{net}}\ \text{ and }\ \mu_{\text{net}}(m)\cdot\mu_{\text{net}}(m+1)=\mu_{\text{net}}^2\cos(\Phi)\ . \tag{17}$$

There are several salient points. First, the data analysis shows that the phase shift across the Y layers is a multiple of π within experimental uncertainty. This is consistent with a scalar coupling through the Y (the Dy spins on either side of the Y layer simply align or antialign). However, scalar coupling is not sufficient to preserve the handedness (helicity) of the helix in the Dy layers across the Y without which the magnetic coherence length would be limited to a single layer. Scalar Ruderman-Kittel-Kasuya-Yosida (RKKY) coupling would require some additional mechanism for the helical coherence other than a conduction-band spin-density wave. Investigation of superlattices with different thicknesses for the Y layer in order to clarify this point is presently underway. Second, the turn angle in the Y layer (ω_Y) is temperature independent at about $52°=0.29\pi$ (equivalent to a modulation

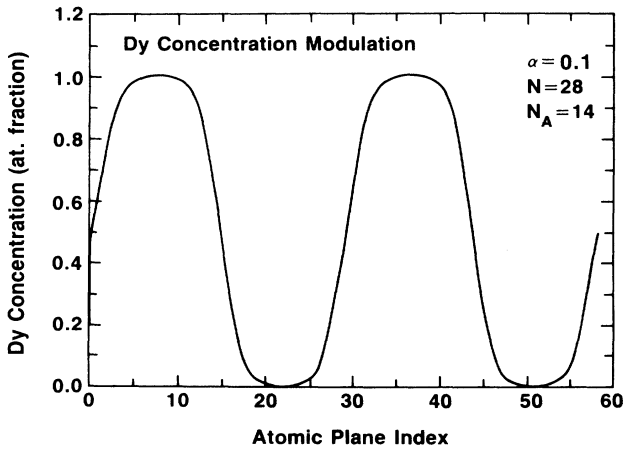

FIG. 6. The concentration modulation obtained for sample A assuming a diffusion model is plotted against the atomic-plane number. The interface is observed to be smeared over about four atomic planes.

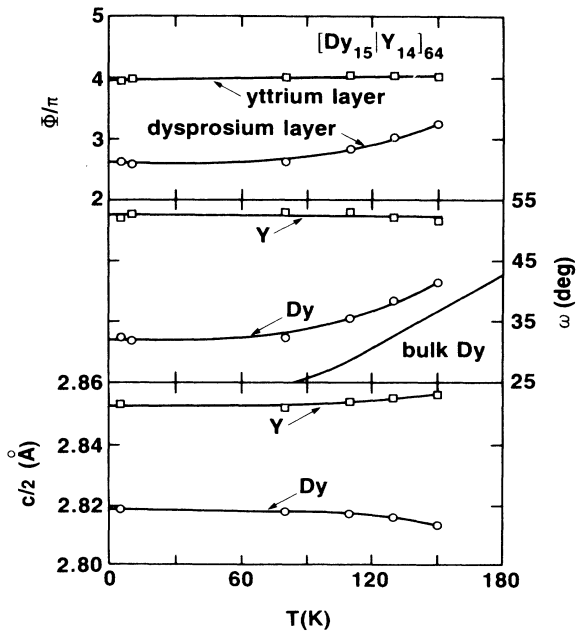

FIG. 7. The parameters obtained from the detailed fits of the observed peak intensities to a model for the superlattice structure factors are plotted vs the temperature. The total magnetic phase shift across the Y layer, Φ_Y, is observed to be a multiple of π (see text). The total phase shift across the Dy layer, Φ_{Dy}, has simply the temperature dependence of the Dy turn angle. The turn angles in the Dy and Y layers, ω_{Dy} and ω_Y, respectively, are quite similar to the values in their bulk counterparts. The separate Dy- and Y-layer interplanar spacings d_{Dy} and d_Y are also plotted vs the temperature. The Dy c-axis lattice parameter expands while the Y lattice contracts with decreasing temperature.

TABLE II. Effective mosaic widths for $[Dy_{15}|Y_{14}]$.

	Q (Å^{-1})					
	1.9590	2.0360	2.3997	2.4787	2.2172	2.2957
Mosaic (min of arc)	36.6	36.8	37.2	38.3	34.0	45.0
Width	mag	mag	mag	mag	nuc	nuc

wave vector of 0.31 Å^{-1}), which is the value obtained in many dilute alloys of rare earths in Y.[9,10,21] The temperature independence of ω_Y follows from the absence of local moments in Y.[20] Third, the turn angle obtained for the Dy layer, ω_{Dy}, has a temperature dependence which is qualitatively similar to bulk Dy. However, the turn angle saturates at low temperatures at about 0.175π (31.5°), while in bulk Dy the value just above the ferromagnetic transition temperature is 0.147π (27°). This value is representative of the center of the Dy layer, while the average turn angle is about 33.5° $[\Phi_{Dy}/(N_A-1]$. The average turn angle is relatively insensitive to our modeling of the interface. This suggests that there is no lock-in transition to $\pi/6$ at low temperatures in this sample. We remark that in bulk Ho a lock-in transition to $\pi/6$ has been observed to be highly sample dependent.[22]

The behavior of the separate Dy and Y lattice parameters again suggests that the zero-field magnetostriction in this superlattice is quite different from that in bulk Dy. The temperature dependence below T_N indicates that the Dy layer gains some volume magnetostrictive energy while the Y lattice contracts normally along the c axis. The Dy and Y layers are thus qualitatively similar to the bulk materials in this regard, although the magnitudes of the length changes are considerably reduced (compare with Fig. 4) due to the elastic coupling at the interfaces with the substrate and between the layers. There is no dramatic increase in the Dy lattice parameter in zero field at any temperature, as would be expected at a ferromagnetic transition. Our field-dependent studies in the next section will further elucidate this behavior.

The Dy moment associated with the long-range helimagnetic order saturates at low temperature as shown in Fig. 8, at about $7.6\mu_B$ (μ_B denotes Bohr magneton), which is well below the free-ion value for Dy. The values of the moment are compared to the $J=\frac{15}{2}$ Brillouin function for the spontaneous magnetization, as in Fig. 5. The "missing" moment below about 80 K appears as short-range ferromagnetic order represented by scattering centered at τ_0, as indicated by the cross hatching in the 10-K data in Fig. 9. Fitting these data with Gaussians shows that it has a Q width of about 0.2 Å^{-1}, which translates into a correlation range which is approximately equivalent to the thickness of a single Dy layer (about 30 Å). It is difficult to make an accurate determination of the intensity in the short-range-order peak, although the comparison between the total-intensity and Dy-moment plots in Figs. 5 and 8 suggest that this short-range order should account for the "missing" moment. It is not yet clear whether this short-range ferromagnetism is intrinsic to the super-

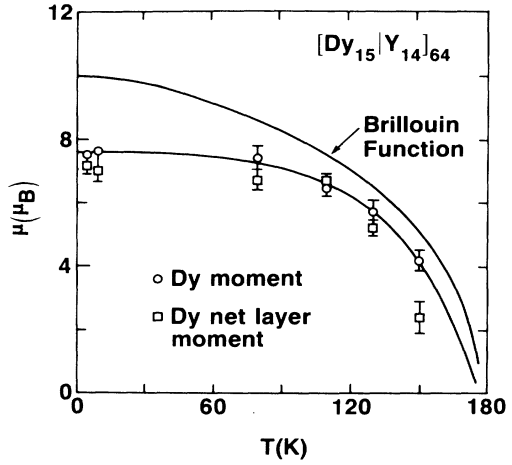

FIG. 8. The Dy moment contributing to the long-range helimagnetism is shown as function of the temperature. The free-ion value of $10\mu_B$ is not obtained at low temperatures, indicating that not all of the spins contribute to the long-range-ordered state. The $J=\frac{15}{2}$ Brillouin function is plotted for comparison. The uncompensated Dy-layer moment is also shown to have approximately the value of a single Dy moment at all temperatures.

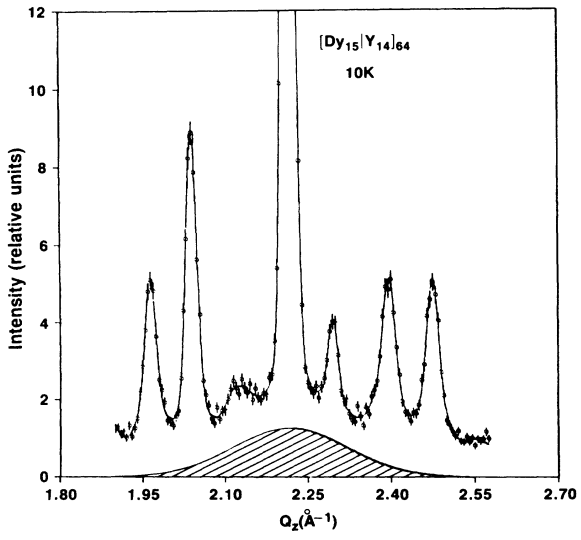

FIG. 9. The missing Dy moment at 10 K in sample A appears as short-range ferromagnetic correlations represented by the cross-hatched intensity centered on the primary Bragg peak.

lattice (it could be, for example, simply the result of impurity pinning of the Dy moments). If one attempts to explain the reduction of the Dy moment as thermal or static disorder at the interfaces, then it is difficult to understand how the long-range helical order is maintained.

Finally, we plot the uncompensated (net) magnetic moment per Dy layer in Fig. 8 as determined from the least-squares fits to the observed peak intensities. This net moment obtains about the same values as a single Dy atom. We shall refer to this figure in the next section, describing the behavior in a magnetic field.

V. FIELD-DEPENDENT DIFFRACTION

A. Field-induced ferromagnetism

The marked differences observed between field-cooled (FC) and zero-field-cooled (ZFC) magnetizations[2] and the absence of a zero-field ferromagnetic transition have prompted us to determine by neutron diffraction the magnetic structure of these superlattices in an applied field.

We first essay a replication of the bulk magnetization measurements[2] by observing the field dependence of the intensity of the primary Bragg peak, τ_0. The square roots of the observed magnetic intensities have been scaled so that the saturation at low temperatures for sample A corresponds to a Dy moment of $10\mu_B$. The resulting isotherms are shown in Fig. 10 for both samples, and were collected by varying the magnetic field along the superlattice $[11\bar{2}0]$ and $[10\bar{1}0]$ basal-plane directions with the spectrometer angles fixed at the zero-field Bragg-peak settings. Magnetometer data are shown for comparison, and where the data overlap there is good agreement for the shape of the magnetization curves. The neutron results seem to indicate a sharper transition to the ferromagnetic state in the 130-K data than the bulk measurements. We have not been able to explain this discrepancy.

Scans through τ_0 in zero field and 25 kOe applied along an easy axis of magnetization are shown in Fig. 11. Our model calculation for the structure factor shows that for small lattice mismatch (as in the present case) the intensity at τ_0 is very insensitive to the lattice mismatch d_{AB} as well as the effective amount of interlayer diffusion, α. Thus the nuclear and magnetic intensities at τ_0 are deter-

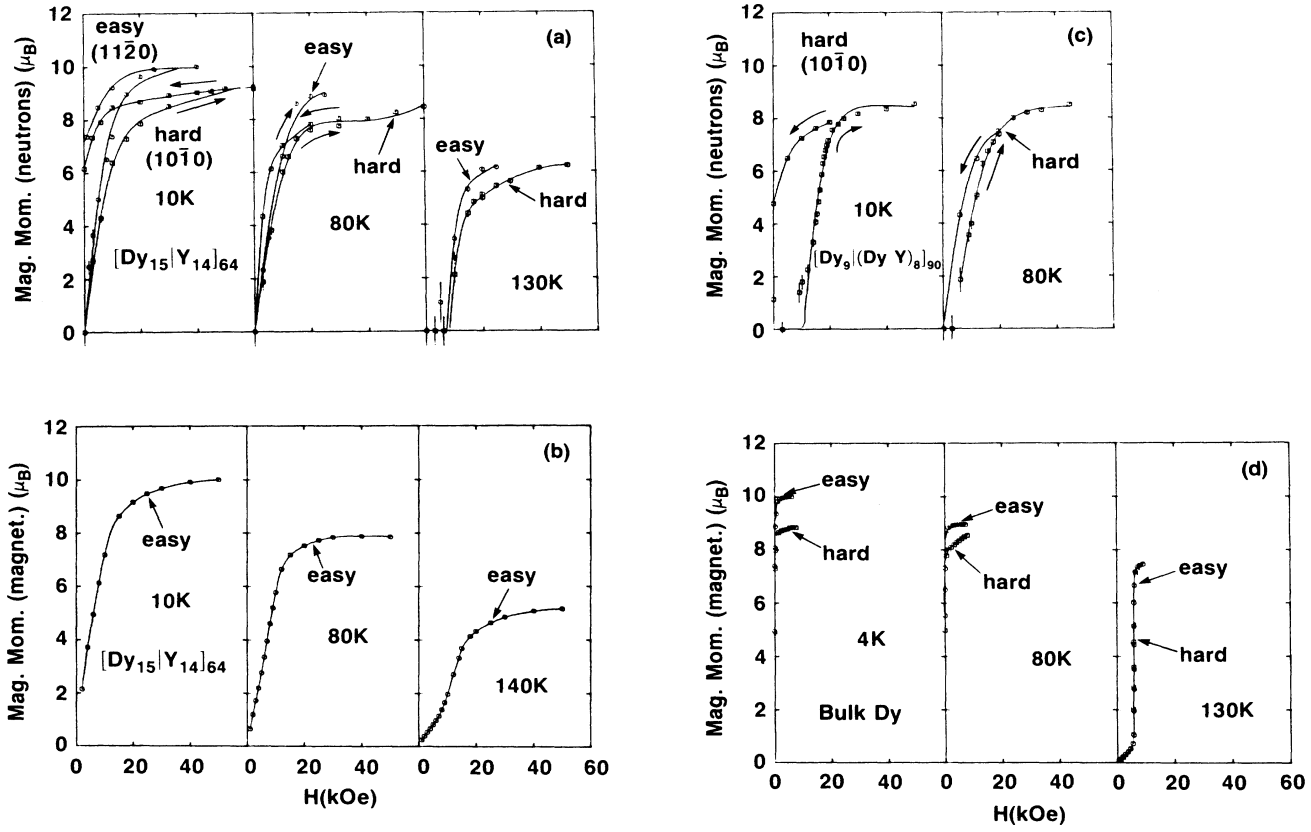

FIG. 10. The magnetization for fields applied along the easy and hard directions in the basal plane of sample A are shown in Fig. (a). These results are in qualitative agreement with magnetometer measurements on the same sample in (b). The basal-plane anisotropy is observed to be similar to that of bulk Dy shown in (d). At low temperatures the slope of the curves is clearly not demagnetization limited, and the first-order transition from the helimagnetic to ferromagnetic states in bulk Dy is not as sharp in the superlattice. A large remanent magnetization remains upon removing the field at low temperatures in both samples A and B [(a) and (c)].

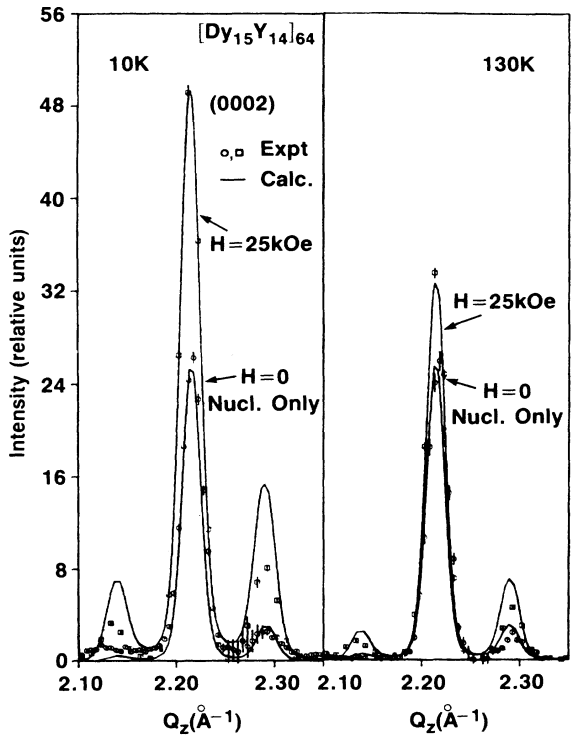

FIG. 11. The [000*l*] scans through the primary Bragg peak are shown for sample A at 10 and 130 K for fields of 0 and 25 kOe. The factor-of-2 increase in the Bragg intensity at 10 K in 25 kOe corresponds to a $10\mu_B$ Dy moment. The induced ferromagnetism is long range since the peak width of the magnetic intensity is identical to the nuclear-intensity peak width.

mined by the relative layer thicknesses and the nuclear and magnetic scattering amplitudes. We assume that the saturation magnetization at 10 K is equivalent to $10\mu_B$ on the Dy atoms in order to determine the relative thicknesses of the Dy and Y layers (note that there is no contribution from conduction-band polarization at τ_0). The observed ratio of magnetic to nuclear intensities is 1.00 ± 0.02, which gives a Dy-layer thickness of 14.8 ± 0.3. This is consistent with α-step measurements[2] of the layer thickness and validates our assumption for the saturation Dy moment.

The scans through τ_0 also confirm that the Bragg-peak width is constant (there is a slight increase in the width during the initial magnetization, but the widths are identical for 0 and 25 kOe). The position of τ_0 shifts by at most 25% of the resolution width. These considerations show that our measurements of the peak height at fixed $Q=\tau_0$ will give a very good representation of the peak intensity.

The isotherms for the magnetization of bulk Dy (Ref. 23) are added to Fig. 10 for comparison with the superlattice curves. The most conspicuous difference between the Dy and superlattice curves is the absence of first-order jumps in the latter. The slopes of the superlattice curves at the initial magnetization are certainly not demagnetization limited. This confirms that these samples are not ferromagnets in zero field at low temperature, as noted previously from the temperature independence of the τ_0 intensity. The basal-plane anisotropy is observed to be qualitatively similar to that found in bulk Dy with $[11\bar{2}0]$ the easy axis of magnetization. This similarity is not surprising, since the single-ion anisotropy depends on the crystalline electric fields, which can only be very different from bulk Dy at the superlattice interface. The different results along the hard and easy directions at 130 K are surprising, since the basal-plane anisotropy should be completely negligible at that temperature (as in the bulk Dy measurements). This may indicate that the elastic properties of the substrate materials, which do not have sixfold basal-plane symmetry, are affecting the forced magnetostriction.

Once ferromagnetic alignment of the spins is obtained at low temperatures (10 K in Fig. 10), there is a considerable remanent magnetization when the field is removed. The observed remanence for a field applied along the hard direction is approximately $\sqrt{3}/2$, as expected if the spins relax to the two nearby easy directions. Note that the remanence is greater if the field is applied along an easy direction. In that case the spins are predominantly trapped along a single easy direction. The remanent ferromagnetic state is long range in nature since the Bragg peak retains its zero-field width. We will also show that the remanent state includes short-range correlations. Although no remanence is found at 80 K in either sample, the magnetization and demagnetization curves do not overlap.

The *c*-axis magnetostriction of sample A has been obtained from the temperature and field dependence of the position of τ_0. These results are shown in Fig. 12. The

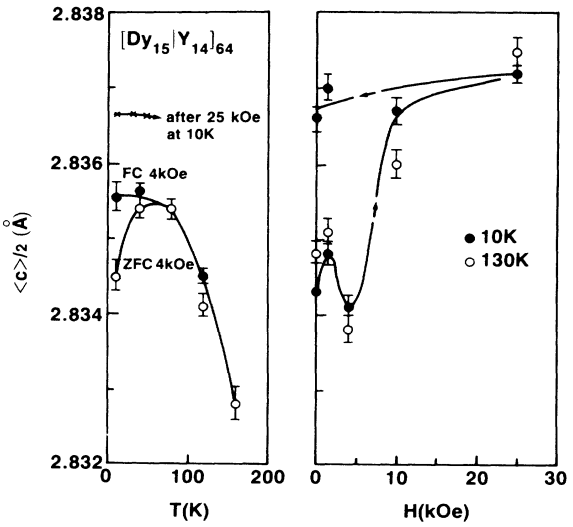

FIG. 12. The average interplanar spacing of sample A is shown as a function of temperature in an applied field of 4 kOe, and as a function of applied field at low and high temperatures. The irreversibility in the magnetostriction occurs in the same temperature regime as found for the magnetization (Fig. 10). The superlattice forced magnetostriction at 25 kOe is half the expansion of bulk Dy at its ferromagnetic transition.

c-axis forced magnetostriction becomes irreversible in the same temperature regime as the magnetization. The expansion of the superlattice along the c axis in a field of 25 kOe is 0.1%, which is half the expansion of Dy at its ferromagnetic transition.[18]

We suggest that the differences in the magnetization arise primarily from the decreased magnetoelastic energy density of the superlattice compared to bulk Dy (the magnetic moment density is lower because of the presence of the Y or $Dy_{0.5}Y_{0.5}$ interlayers as well as the substrate). The ferromagnetic transition in bulk Dy is driven by the gain of magnetoelastic energy in the ferromagnetic state compared to the helimagnetic state, which arises principally from an orthorhombic distortion of the lattice along the broken-symmetry direction.[3,4] This energy gain is sufficient to overcome the resulting increase in the elastic strain energy. However, the addition of the superlattice interlayers and the substrate makes it too costly in terms of strain energy for the ferromagnetic basal-plane distortions to occur. The c-axis expansion is still allowed. Of course, when a sufficient magnetic field is applied the energy balance can be shifted to favor the ferromagnetic state once more. The fact that the fields required to achieve magnetic saturation are considerably higher in the superlattice than in bulk Dy at equivalent temperatures is evidence for this difference in strain energy. We also suspect that the magnetization process may become continuous as the result of strain modulation.

B. Driving energy for ferromagnetism in the superlattice

We attempt to support these remarks by a quantitative calculation of the driving energy for ferromagnetism in the superlattice using the bulk values of the relevant parameters for Dy and Y. The relevant terms in the driving energy density for ferromagnetism are the single-ion–anisotropy, exchange, and magnetoelastic energies:

$$f_d = \Delta f_{\rm an} + \Delta f_{\rm ex} + \Delta f_{\rm me} \ . \tag{18}$$

The driving-energy density is the term-by-term difference in the free-energy density between the ferromagnetic and helimagnetic states, $\Delta f_\mu = f_\mu(\text{helix}) - f_\mu(\text{FM})$, with f_d becoming positive when the ferromagnetic state is favored. We shall for the moment neglect the anisotropy term. The exchange term in f_d for bulk Dy is about -1.0 K/atom at T_c and is only weakly temperature dependent (favoring the helimagnetic state).[3,4] Cooper[3] has estimated $\Delta f_{\rm me}$ at $T=0$ K in bulk Dy to be about 2.0 K/atom, which then renormalizes to about half this value at the ferromagnetic transition. This energy cannot be gained until the system is ferromagnetic (the lattice-clamping effect), which makes the transition discontinuous. In order to reestimate $\Delta f_{\rm me}$ for the superlattice, we follow Evenson and Liu[4] and separate $f_{\rm me}$ into elastic and magnetoelastic terms. If the superlattice were free from a substrate, then the only additional term would be the elastic energy density of the Y layer. The dominant contribution to the driving energy would arise from the γ strains as in bulk Dy, corresponding to the distortion of the circular symmetry of the basal plane, which occurs in the ferromagnetic state. However, if the γ strain in the superlattice forces a coherent γ strain in the substrate, then a term proportional to the volume of the substrate and the strain squared will be added to the elastic energy. Since the sapphire substrate in the present case is 4 orders of magnitude larger in volume than the sample, any strains in the plane of the sample will be very unfavorable energetically. We shall thus calculate the magnetoelastic energy, allowing only a c-axis anomalous strain in the Dy layers. The conventional expression for the elastic energy in a hexagonal system is

$$f_{\rm el} = \tfrac{1}{2}[c_{11}^{\alpha}(\epsilon^{\alpha,1})^2 + c_{22}^{\alpha}(\epsilon^{\alpha,2})^2 + c_{\gamma}(\epsilon^{\gamma})^2] \ . \tag{19}$$

The $\epsilon^{\alpha,1}$ strain mode is a pure volume expansion, while the $\epsilon^{\alpha,2}$ mode is a linear combination of a circular basal-plane contraction and a c-axis expansion. The ϵ^{γ} mode is the orthorhombic basal-plane distortion. We can retain this formalism in the present case by restricting $\epsilon^{\gamma}=0=\epsilon^{\alpha,1}-\sqrt{3}\epsilon^{\alpha,2}$, so that all basal-plane strains are zero, and $\epsilon^{\alpha,1}=\epsilon^{z}$ (the c-axis strain). Keeping only the one- and two-ion terms as in Ref. 4, the magnetoelastic energy density can be expressed as

$$f_{\rm me} = \tfrac{1}{2}\tilde{c}^{\,\alpha}(\epsilon^{z})^2 - \tilde{A}^{\,\alpha}(\cos\omega)(\epsilon^{z}) \ , \tag{20}$$

where

$$\tilde{c}^{\,\alpha} = c_{11}^{\alpha} + \tfrac{1}{3}c_{22}^{\alpha} \quad \text{and} \quad \tilde{A}^{\,\alpha} = c_{11}^{\alpha}\lambda_1 + \frac{1}{\sqrt{3}}c_{22}^{\alpha}\lambda_2 \ , \tag{21}$$

and the strains λ_1 and λ_2 are defined in Ref. 4. Solving for the equilibrium strains in the superlattice results in the expression for the magnetoelastic driving energy for ferromagnetism:

$$\Delta f_{\rm me} = \tfrac{1}{2}(\sin^2\omega)(\tilde{A}^{\,\alpha})^2/\tilde{c}^{\,\alpha} \ . \tag{22}$$

The values at $T=10$ K for the anomalous expansion in ferromagnetic bulk Dy (Refs. 18, 24, and 25) (where λ_1 and λ_2 are just the α strains) are $\lambda_1=0.0009$ and $\lambda_2=0.0049$, while the elastic constants are $c_{11}^{\alpha}=4.2\times10^{11}$ ergs/cm^3 and $c_{22}^{\alpha}=13.1\times10^{11}$ ergs/cm^3.[26] Using $\omega=30°$ we find that $\Delta f_{\rm me}(10\text{ K})=0.6$ K/atom, favoring ferromagnetism. Therefore, even at low temperatures the magnetoelastic energy is not sufficient to overcome the exchange-energy barrier of -1.0 K/atom in any Dy thin film elastically constrained by a much thicker substrate. Also, we obtain the equilibrium strain $\epsilon^{z}=(\tilde{A}^{\,\alpha}/\tilde{c}^{\,\alpha})\cos(\omega)$, so that the forced magnetostriction at 10 K is calculated to be 6.3×10^{-4}. This compares favorably with the observed value of 9.0×10^{-4} shown in Fig. 12. We are presently unable to reconcile these calculations with magnetization measurements on a MBE-grown sample of pure Dy, which showed the behavior of bulk Dy in an applied field of 1 kOe.[2] If the superlattice is freed from the substrate, then a similar calculation shows that the basal-plane strain terms contribute enough energy to drive the superlattice ferromagnetic at low temperatures. The γ-strain term alone would be

$$\Delta f_{\rm me} = \tfrac{1}{8}(A^{\gamma})^2/\bar{c}^{\gamma}\ , \tag{23}$$

where $\bar{c}^{\gamma} = c^{\gamma}_{\rm Dy} + c^{\gamma}_{\rm Y}$ for a superlattice with equal thicknesses for the Dy and Y layers, and $A^{\gamma} = 2c^{\gamma}_{\rm Dy}\epsilon^{\gamma}$. Using $\epsilon^{\gamma} = 0.0048$ and $c^{\gamma} = 0.27 \times 10^6$ K/atom from Refs. 24 and 26 at 10 K gives $\Delta f_{\rm me} \approx 1.4$ K/atom for the substrate-free superlattice. We also argue that the basal-plane anisotropy, which reaches a value of -2.0 K/atom (Ref. 18) at temperatures on the order of 10 K, may be ineffectual in driving a ferromagnetic transition because of its single-ion character. Although spins prefer to align along an easy-axis direction, there is no coherence of this choice from site to site, since there are six equivalent easy directions. However, a global anisotropy, provided, for example, by a substrate, might break the remaining six-fold symmetry. The principal result of adding the anisotropy is to pin the magnetic configuration to the lattice.

C. Field dependence of the helical state

The field dependence of the magnetic satellites reveals more details of the magnetization process. This dependence is shown at 10 and 130 K for sample A in Fig. 13 with the field along the easy [11$\bar{2}$0] direction (results are similar when the field is applied along the hard direction). First, note that a 1.5-kOe field has no effect on the magnetic satellites at 10 K, although the magnetization shown in Fig. 10 has a considerable nonzero slope at the initial magnetization. The reason for this discrepancy is that at low temperature the magnetization process is initiated by a conversion of the short-range ferromagnetic order into long-range order. However, for fields above about 5 kOe the magnetic satellite intensity gradually decreases as the τ_0 intensity increases. This behavior is consistent with a picture of the magnetization process in which the magnetic helix is gradually distorted towards ferromagnetic alignment. We do not find compelling evidence for a first-order transition to a ferromagnetic or fan state,[27] although there is some structure below 80 K in the hard-direction magnetization (see Fig. 10) similar to that found in holmium.[22] We reiterate our expectation that inhomogeneous strains might well smear out any such sharp transition in the superlattice.

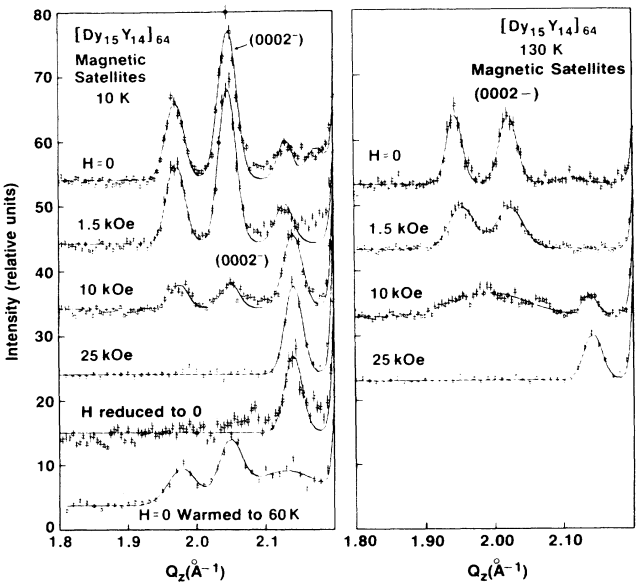

FIG. 13. The field dependence of the helimagnetic state is shown for sample A at temperatures of 10 and 130 K with the field along the easy direction. At low temperature the magnetic satellite intensity decreases for fields above about 1.5 kOe with complete ferromagnetic saturation by 25 kOe. Very little broadening of the magnetic satellites is observed at 10 K. However, at 130 K the first effect of the applied field is to broaden the magnetic satellites, and a field of 10 kOe is sufficient to limit the helimagnetic coherence to a single bilayer. The helimagnetic state is not reformed when the field is removed at low temperature, but can be regained upon warming, although with a shorter coherence length than the zero-field cooled state.

At fixed temperature and for magnetic fields accessible in these experiments, the magnetic satellite positions are unshifted as observed in most rare-earth incommensurate magnetic structures. This is not surprising since the ordering wave vector is determined by the band structure.[20]

At 10 K and with a 25-kOe field along the [11$\bar{2}$0] (easy axis) of sample A, no observable intensity remains at the magnetic satellite positions, in agreement with our finding the full free-ion moment participating in long-range ferromagnetic order. At this point, when the magnetic field is reduced to zero, the ZFC helimagnetic state is not restored. About half of the magnetic intensity remains at the τ_0 position, in agreement with the remanence shown in Fig. 10 of about 70% of the saturation value. The remaining magnetic intensity is diffuse, representing some combination of short-range ferromagnetic correlations and short-range helimagnetic or fan-state correlations. When the temperature is then raised, the remanent magnetization gradually decreases and magnetic intensity is transferred to the original ZFC satellite positions. This behavior, along with our measurements of the anisotropy in Fig. 10, clearly shows that the Dy spins must cross relatively high energy barriers when moving from the ferromagnetic to helimagnetic states, and it is natural to assume that the single-ion basal-plane anisotropy provides those barriers. Note that the low-temperature anisotropy energy of 2.0 K/atom is equivalent to a 2-kOe field applied to $10\mu_B$. It is not surprising that the bulk magnetization[2] shows features which are spin-glass-like, when the presence of anisotropy barriers is taken into account. We are in the process of making a detailed study of the temperature and field dependence of the remanent state to elucidate the precise nature of the energy barriers. The helimagnetic coherence is also significantly shorter ranged in the reformed remanent state than in the ZFC states. We point out that similar remanent states have been observed in bulk Ho (Ref. 22) and in Dy-Y alloys (Ref. 19).

At 130 K the magnetization process for sample A is qualitatively different than at 10 K. Upon applying a magnetic field of 1.5 kOe, the magnetic satellites are observed to broaden. This is quite distinct from the low-temperature behavior where the peaks retain their zero-

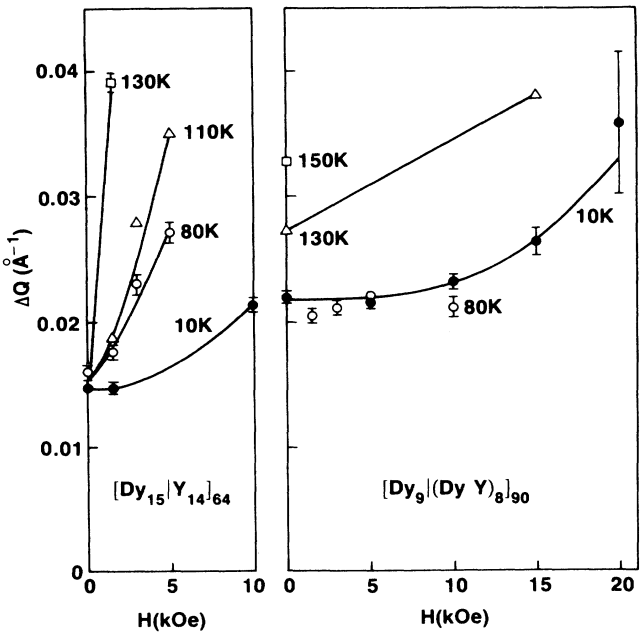

FIG. 14. The intrinsic width of the most intense magnetic satellite is shown as a function of the applied field for samples A and B. At high temperatures in sample A the coherence is destroyed by a random-field coupling of the external field to the uncompensated Dy-layer moment (see text). At low temperatures basal-plane anisotropy prevents an equivalent distortion of the helix. The interlayer coupling is stronger in sample B, where all basal planes are near-neighbor coupled by Dy spins. The applied field is thus not as effective in breaking the helimagnetic coherence.

field width up to about 10 kOe. The full width of the most intense magnetic peak has been plotted as a function of the applied magnetic field for several temperatures in Fig. 14. To our knowledge this rapid destruction of the coherence length has not been observed in any bulk helimagnets. This must therefore be a consequence of the weak interlayer coupling of the Dy spins, along with the rapid decrease of basal-plane anisotropy as the temperature is raised. Our data analysis also gives an uncompensated magnetic moment per layer of Dy of $5.4\mu_B$ at 130 K due to the mismatch of the helix wavelength with the Dy-layer thickness (see Fig. 7). We suggest that the Zeeman energy of the external magnetic field coupled to this excess magnetic moment per layer is sufficient to break the weak interlayer coupling between the Dy spins. The phase shift per bilayer of the net layer moment in zero applied field is just the total bilayer phase shift Φ previously measured [see Eq. (17)]. Thus for magnetic fields small compared to the intralayer exchange, the helical spin arrangement within the Dy layers is unperturbed and we may write the Hamiltonian in terms of the net moment unit vectors $\hat{\mu}_{\rm net}$, as

$$H=-JS^2\sum_m \hat{\mu}^{\dagger}_{\rm net}(m)\cdot R(-\Phi)\cdot\hat{\mu}_{\rm net}(m+1) -g\mu_{\rm net}\mathbf{B}\cdot\sum_m \hat{\mu}_{\rm net}(m)\ . \tag{24}$$

Here, $R(-\Phi)$ is the matrix which rotates $\hat{\mu}_{\rm net}(m+1)$ to be parallel to $\hat{\mu}_{\rm net}(m)$, so that the exchange term favors the angle Φ between the net moment vectors. The weak effective interlayer exchange is represented by J, the magnitude of the Dy spin is S, and $\mathbf{B}$ is the external field. At this point we make the gauge transformation

$$\hat{\mu}_{\rm net}(m)=R(m\Phi)\hat{\mathbf{s}}_m\ , \tag{25}$$

so that the Hamiltonian can be written

$$H=-JS^2\sum_m \hat{\mathbf{s}}_m\cdot\hat{\mathbf{s}}_{m+1}-g\mu_{\rm net}B\sum_m [R(-m\Phi)\hat{\mathbf{B}}]\cdot\hat{\mathbf{s}}_m\ . \tag{26}$$

This form of the Hamiltonian explicitly shows that the uniform external field couples to the uncompensated Dy-layer moments as a random field. That is, $m\Phi$ modulo 2π is a pseudorandom number between zero and 2π provided that Φ modulo 2π is not an integer. Since the $\hat{\mathbf{s}}$ are continuous variables (XY model), random-field theory[28] predicts that the long-range helical order will be destroyed by the external field. We can approximate the strength of the interlayer coupling at 130 K as 5 kOe$\times 5.5\mu_B \approx 1$ K/Dy layer. That is, at 5 kOe the Zeeman energy is approximately equal to the interlayer coupling strength. As the external field is increased, the angles $\Phi_{\rm Y}$ between the $\hat{\mathbf{s}}_m$ become random and the configurational average of $\Phi_{\rm Y}$ approaches zero. If we further assume that the helical order within the Dy layers is unperturbed, then the configurational average of the total bilayer phase shift approaches $\Phi_{\rm Dy}$ ($\langle\Phi\rangle=\langle\Phi_{\rm Y}+\Phi_{\rm Dy}\rangle=\langle\Phi_{\rm Y}\rangle+\langle\Phi_{\rm Dy}\rangle=\Phi_{\rm Dy}$). Single magnetic satellites would be observed on either side of τ_0 with peak widths of about $2\pi/L$. The positions of these peaks would still be given by the total phase shift across the bilayer, Φ. Since, in sample A, $\Phi_{\rm Y}$ is very near to a multiple of 2π, the structure in which the uncompensated layer moments are aligned should show the magnetic satellites at roughly the same positions as the most intense zero-field peaks. This description fits well the observed field dependence of the magnetic satellites at 130 K, with an applied field of 10 kOe leaving a single broad magnetic satellite centered approximately at the positions of the zero-field satellites. The induced moment obtained for fields above 10 kOe is then due to the subsequent distortion of the remaining helical order in the Dy layers. Again, a sensitive test of these conjectures involves a future detailed study of the magnetic structure as a function of the Dy and Y thicknesses.

The field dependence of the magnetic coherence length in sample B is much weaker than in sample A, as expected, since there are nearest-neighbor Dy atoms which couple all of the basal planes. It is interesting that the coherence length in zero field is observed to decrease for temperatures above 110 K in sample B.

The field dependence of the diffraction scan is shown for sample B (the Dy–Dy-Y alloy sample) at 10 K in Fig. 15. In this case the magnetic field is applied along a $[10\bar{1}0]$ direction, and the data are qualitatively similar to the "hard" direction data in Fig. 10, with intensity obtained at τ_0 only for fields above 10 kOe. As previously mentioned, the superlattice peaks are not observed be-

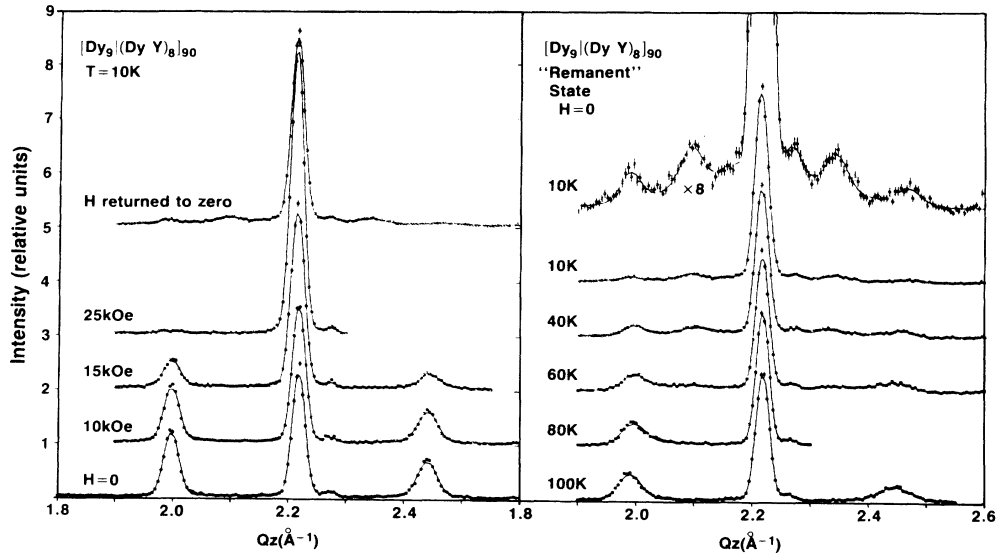

FIG. 15. The field dependence of the helimagnetic state in sample B is shown at a temperature of 10 K. This dependence is similar to that of sample A (Fig. 13). The remanent state has peaks corresponding to both short-range helimagnetic and ferromagnetic order. Again, as in sample A, the helimagnetic state is reformed upon warming, but with a shorter coherence length than the ZFC state.

cause the nuclear and magnetic contrasts are weak. This implies that ferromagnetism is induced in both the Dy and alloy layers as the field is increased. As was the case for sample A, the remanent state obtained by reducing the magnetic field to zero after raising it to 25 kOe is not the same as the ZFC state. A similar remanent magnetization (intensity on τ_0), about 70% of that observed at 25 kOe, is obtained, with only very weak and broad peaks observed at the ZFC magnetic satellite positions. Additional weak, broad peaks also appear between the ZFC satellite peak positions and τ_0. This pattern suggests that in the remanent state in sample B the Dy layers are ferromagnetically aligned, predominantly along the previously applied field direction, while the Dy-Y alloy layers tend towards helical order. This structure could provide sufficient ferromagnetic contrast to make the superlattice satellites of τ_0 observable. The coherence length of this magnetic structure is only several bilayers, since complete coherence with the helical order would require that the ferromagnetically aligned Dy layers relax across strong anisotropy barriers. In fact, the coherent state which is obtained once this relaxation is allowed to take place by raising the temperature is just the ZFC state with a reduced coherence length. This behavior of the remanent state is also shown in Fig. 15. Overall, we find that the magnetic states and magnetization process are quite similar in samples A and B. The greatest difference between the two samples is in the breakdown of helimagnetic coherence in an applied field.

VI. CONCLUSION

We have shown by neutron diffraction that it is possible to characterize the magnetic structures in single-crystal superlattices by means of a simple model for the superlattice structure factor. In the Dy-Y superlattices investigated here the measurements show that the magnetic structure is modulated by the separate magnetic properties of each layer type. In sample A the helimagnetic turn angle in the Y layers is consistent with the 52° value obtained in dilute alloys and other superlattices[7–10] as well as band-structure calculations.[29] The turn angle in the Dy layers is qualitatively similar to that of bulk Dy, varying from about 45° near T_N to about 31.5° at 10 K (the bulk Dy value is about 27° at T_c). The phase coherence of the ordered magnetic state extends across 4–5 bilayers. This implies that the helicity is maintained across the 38-Å yttrium layers, which, in turn, argues for the stabilization of a conduction-band spin-density wave in the Y. A simple scalar RKKY coupling is ruled out unless there is some intrinsic factor which maintains the same helicity in separate Dy layers.

The properties of these superlattices in an applied magnetic field are quite different from those of bulk Dy. The discrepancies can largely be ascribed to the very different magnetoelastic energy density of the superlattice compared to bulk Dy. The γ magnetostriction which drives the first-order ferromagnetic phase transition in bulk Dy is clamped, so that the zero-field-cooled states are always helimagnetic. The application of a magnetic field then produces a smeared second-order-like transition to a ferromagnetic state. At 10 K the single-ion basal-plane anisotropy of Dy becomes sufficient to metastably freeze the ferromagnetic state, and the ZFC helimagnetic states cannot be recovered until the temperature is warmed above about 40 K.

At high temperatures (130 K$=0.76T_N$) the magnetization process includes a gradual reduction of the magnetic phase coherence. This is a phenomenon unique to the superlattices, and is likely due to the weak interlayer cou-

pling compared to the Zeeman energy of the uncompensated Dy-layer moment in an applied field. Since the initial loss of coherence in only 1.5 kOe produces no observable intensity on the nuclear Bragg peak τ_0, we postulate that the external field randomly twists the helix sections in each Dy layer. The interlayer coupling strength in sample A across the 38 Å of yttrium is then estimated at 1 K per Dy layer per basal-plane atom.

Many of the interesting and new features of these superlattice magnets can only be further investigated by pursuing a detailed investigation of the dependence of the magnetic structure and properties on the separate Dy and Y thicknesses. These studies are presently underway.

ACKNOWLEDGMENTS

We would like to acknowledge insightful discussions with R. J. Kwo and C. F. Majkrzak on their related work with Gd-Y superlattices, and A. Overhauser and A. R. Mackintosh on the details of spin-density waves. Work at the University of Illinois was supported by the Materials Research Program of the National Science Foundation (NSF) under Grant No. DMR-82-16981 and by the Solid State Physics Section of the NSF under Grant No. DMR-85-21616. One of us (J.B.) was partially supported by IBM.

*Present address: AT&T Bell Laboratories, Holmdel, NJ 07733.

[1]J. Kwo, D. B. McWhan, M. Hong, E. M. Gyorgy, L. C. Feldman, and J. E. Cunningham, in *Layered Structures, Epitaxy, and Interfaces,* Materials Research Society Symposia Proceedings No. 37, edited by J. H. Gibson and L. R. Dawson (Materials Research Society, Pittsburgh, 1985), p. 509.

[2]S. Sinha, J. Cunningham, R. Du, M. B. Salamon, and C. P. Flynn, in *Proceedings of the International Conference on Magnetism,* edited by J. J. Rhyne, B. R. Cooper, D. L. Huber, N. C. Koon, and R. C. O'Handley (North-Holland, Amsterdam, 1985); J. Borchers, S. Sinha, M. B. Salamon, R. Du, and C. P. Flynn, J. Appl. Phys. (to be published).

[3]B. R. Cooper, Phys. Rev. **169**, 281 (1968); B. R. Cooper, Phys. Rev. Lett. **19**, 900 (1967).

[4]W. E. Evenson and S. H. Liu, Phys. Rev. **178**, 783 (1969).

[5]J. J. Rhyne, R. W. Erwin, M. B. Salamon, Shantanu Sinha, J. Borchers, J. E. Cunnningham, and C. P. Flynn, Less-Common Met. (to be published).

[6]See also M. B. Salamon, Shantanu Sinha, J. J. Rhyne, J. E. Cunningham, R. W. Erwin, J. Borchers, and C. P. Flynn, Phys. Rev. Lett. **56**, 259 (1986).

[7]J. Kwo, E. M. Gyorgy, D. B. McWhan, M. Hong, F. J. DiSalvo, C. Vettier, and J. E. Bower, Phys. Rev. Lett. **55**, 1402 (1985); J. Kwo, E. M. Gyorgy, F. J. DiSalvo, M. Hong, Y. Yafet, and D. B. McWhan, J. Magn. Magn. Mater. **74-77**, 771 (1986).

[8]C. F. Majkrzak, J. W. Cable, J. Kwo, M. Hong, D. B. McWhan, Y. Yafet, J. V. Waszczak, and C. Vettier, Phys. Rev. Lett. **56**, 2700 (1986).

[9]L. E. Wenger, G. W. Hunter, J. A. Mydosh, J. A. Gotaas, and J. J. Rhyne, Phys. Rev. Lett. **56**, 1090 (1986).

[10]L. J. P. Ketelson and M. B. Salamon, Solid State Commun. **55**, 237 (1985); B. D. Rainford, H. B. Stanley, and B. V. B. Sarkissian, Physica **130B**, 388 (1985).

[11]G. E. Bacon, *Neutron Diffraction* (Clarendon, Oxford, 1975), p. 67.

[12]J. D. Axe and J. B. Hastings, Acta Crystallogr. Sect. A **39**, 593 (1983).

[13]M. Iizumi, Jpn. J. Appl. Phys. **12**, 167 (1973).

[14]D. B. McWhan, in *Synthetically Modulated Structures,* edited by L. Chang and B. C. Giessen (Academic, New York, 1985), p. 43; K. E. Meyer, G. P. Felcher, S. K. Sinha and Ivan K. Schuller, J. Appl. Phys. **52**, 6608 (1981).

[15]E. M. Gyorgy, D. B. McWhan, J. F. Dillon, Jr., L. R. Walker, and J. V. Waszczak, Phys. Rev. B **25**, 6739 (1982).

[16]A. Segmuller and A. E. Blakeslee, J. Appl. Crystallogr. **6**, 19 (1973).

[17]P. Scherrer, Gött. Nachr. **2**, 98 (1918).

[18]J. J. Rhyne and S. Legvold, Phys. Rev. **138**, A507 (1965).

[19]S. Weinstein, R. S. Craig, and W. E. Wallace, J. Appl. Phys. **34**, 1354 (1963).

[20]A. J. Freeman, in *Magnetic Properties of Rare-Earth Metals,* edited by R. J. Elliot (Plenum, New York, 1972), p. 314, and references therein.

[21]W. C. Koehler, in *Magnetic Properties of Rare-Earth Metals,* Ref. 20, p. 94.

[22]W. C. Koehler, J. W. Cable, H. R. Child, M. K. Wilkinson, and O. E. Wollan, Phys. Rev. **158**, 450 (1967).

[23]D. R. Behrendt, S. Legvold, and F. H. Spedding, Phys. Rev. **109**, 1544 (1958).

[24]F. J. Darnell and E. P. Moore, J. Appl. Phys. **34**, 1337 (1963).

[25]E. Callen and H. B. Callen, Phys. Rev. **139**, A455 (1965); E. Callen, J. Appl. Phys. **39**, 519 (1968).

[26]M. Rosen and H. Klimer, Phys. Rev. B **1**, 3748 (1970).

[27]T. Nagamiya, K. Nagata, and Y. Kitano, Prog. Theor. Phys. **27**, 1253 (1962); Y. Kitano and T. Nagamiya, *ibid.* **31**, 1 (1964).

[28]Y. Imry and S.-k. Ma, Phys. Rev. Lett. **35**, 1399 (1975).

[29]S. H. Liu, R. P. Gupta, and S. K. Sinha, Phys. Rev. B **4**, 1100 (1971).